

Calibration of Wavefront Phase Image Using Phase-Shifting Iteration Algorithm in Quadriwave Lateral Shearing Interferometry

Bochuan CUI

University of Chinese Academy of Sciences, Beijing 100000, China

Tao CHEN, Jianli WANG* and Kainan YAO

*Changchun Institute of Optics, Fine Mechanics and Physics,
Chinese Academy of Sciences, Jilin 130033, China*

(Received 20 June 2017, in final form 14 August 2017)

A phase-shifting iterative algorithm is proposed to calibrate the wavefront phase image demodulated from an interferogram generated by quadriwave lateral shearing interferometer. It reduces the error of the residual slope to $RMS < 1.5 \times 10^{-4} \lambda$ after calibration. A favorable result was obtained in the present experiment. We measured a certain wavefront provided by a deformable mirror using the quadriwave lateral shearing interferometer after calibration. The deviation between the wavefront graph of the deformable mirror and the wavefront constructed by quadriwave lateral shearing interferometer was 2.63%. Our method increases the accuracy and reliability of the reconstructed wavefront data and has a high practical value, all of which meets the requirement of high-precision wavefront sensing.

PACS numbers: 42.25.Hz, 82.20.-w, 68.43.-h

Keywords: Interferometry, Wavefront sensor, Calibration

DOI: 10.3938/jkps.72.359

I. INTRODUCTION

The concept of the quadriwave lateral shearing interferometry (QWLSI) was proposed in 2000 and is based on the interference of four tilted replicas of the wavefront to be analyzed [1–4]. A number of the research into QWLSI applications began in the next few years. Many quadriwave lateral shearing interferometers working on various wavelength had been developed, such as X-rays [5], extreme ultraviolet [6–8] and infrared wavelengths from 2 to 16 μm [9,10]. In 2015, a paper reviewed the recent developments in IR metrology using quadriwave lateral shearing interferometry and stated that Phasics has developed wave front sensors compatible with wavelengths ranging from 193 nm to 14 μm [11]. There are some applications in beam quality evaluation, such as the measurement of the relative piston between two independent beams [12] and the collective phase measurement of an array of fiber lasers [13]. The QWLSI also has important applications in the field of microscopy, which is called quantitative phase imaging (QPI). In 2009, a research got a lateral resolution up to the microscope diffraction limit with 300×400 images and a huge OPD sensitivity of less than 1 nm and the implementation sim-

plicity [14]. In 2011, A thermal image of nanostructures was got by QWLSI [15]. In 2015, a new technique combines quantitative phase images with varying polarization excitation to create retardance images which called quantitative retardance imaging (QRI) was described [16]. The approach was applied to collagen fibers leading to a birefringence value of $(3.4 \pm 0.3) \times 10^{-3}$ and to living cells, showing that cytoskeleton can be imaged label-free. Recently, a new type of randomly encoded hybrid grating (REHG) for wavefront testing by quadriwave lateral shearing interferometry was proposed [17]. Compared with the modified Hartmann mask (MHM), only four diffraction orders exist in its diffraction field, and the quadriwave lateral shearing interferometry is better achieved. In 2017, a wideband sensitivity-enhanced interferometric microscopy was reported for quantitative phase imaging in real time by employing two quadriwave lateral shearing interferometers based on REHG with different lateral shears [18].

The QWLSI offers the crucial advantage that it yields an analyzed wavefront without the use of a reference arm and consequent time consuming alignment. It combines fundamental properties, such as the achromaticity the high resolution, the adjustable sensitivity and dynamic, to a great versatility. Due to these qualities, the QWLSI is an excellent candidate to perform high quality wavefront measurements in hard context. However, there's a

*E-mail: wangjianli@ciomp.ac.cn

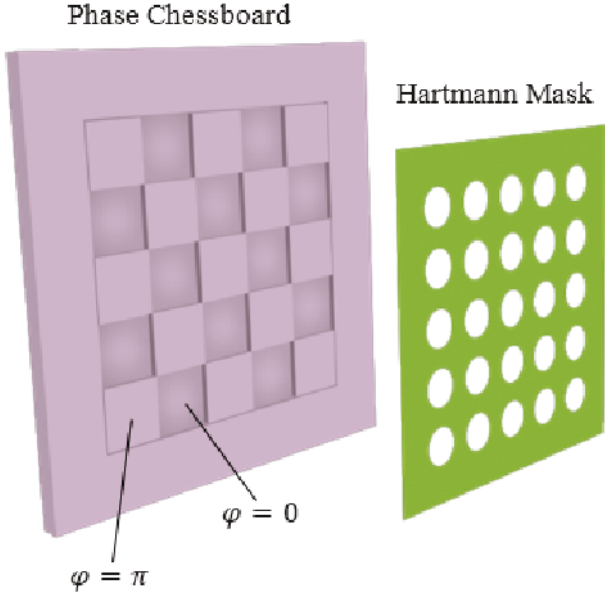


Fig. 1. (Color online) Construction of MHM.

problem that cannot be ignored. The problem is that when a new quadriwave lateral shearing interferometer was manufactured. There are some inherent errors in the device, including the etching error of grating and the position error of internal component. These errors will reduce the accuracy of phase imaging, and must be resolved by a means of calibration. The inherent error of the device will mainly lead to gradient error in the phase image and phase-shifting algorithm is an effective means to solve it. Phase-shifting algorithm was firstly proposed by Kenichi Hibino [19] to compensate the phase error in nonsinusoidal waveforms. Then a new phase-shifting algorithm called a double three-step algorithm was developed to reduce the measurement error of a three-dimensional shape measurement system [20]. It also had been used in phase-shifting digital fringe projection profilometry [21], fringe projector based on beamshaping [22] and 3D phase-shifting fringe projection system [23].

In this paper, we proposed an improved phase-shifting algorithm to calibrate the quadriwave lateral shearing interferometer. A polynomial fitting method is used to calculate the tilt of the phase image. The obtained tilt is used as a parameter for phase shifting to compensate the errors in the phase image. The iterative method is further used to reduce the residuals to a fairly small value. This method solves the problem of the device errors and helps to a higher accuracy phase imaging.

II. PRINCIPLE

Quadriwave lateral shearing interferometry uses a MHM, which combines a Hartmann mask with a phase

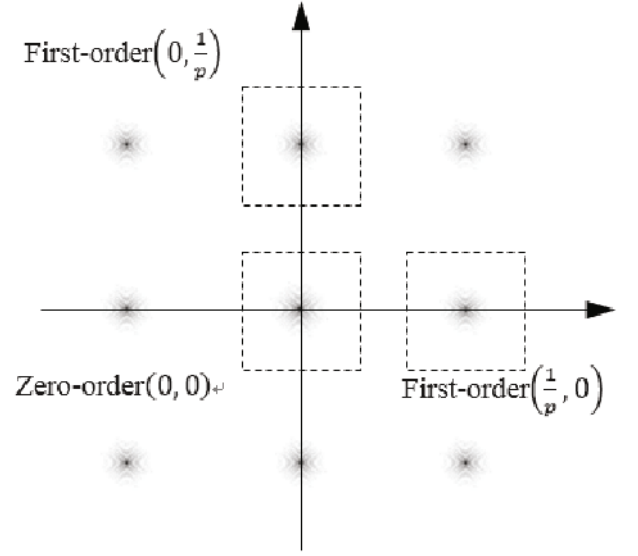


Fig. 2. Fourier spectrum of an interferogram.

chessboard. The MHM divides light into four diffracted beams, making them interfere with each other. Specifically, the period of phase chessboard is twice as much as that of the Hartmann mask, and its phase gap between the adjacent grid is π . The radius of aperture of the Hartmann mask is 0.67 times of its period. The structure of MHM is shown in Fig. 1.

If we only consider the $(\pm 1, \pm 1)$ order of the diffracted beam, the amplitude transmittance of MHM is:

$$t(x, y) = \cos\left(\frac{\pi x}{p}\right) \cos\left(\frac{\pi y}{p}\right), \quad (1)$$

where (x, y) is the spatial coordinate and p is the stop period. Then, the corresponding light intensity transmission is

$$T(x, y) = \frac{1}{4} \left\{ 1 + \left[\cos\left(\frac{2\pi}{p}x\right) + \cos\left(\frac{2\pi}{p}y\right) \right] + \frac{1}{2} \left[\cos\left(\frac{2\pi}{p}(x+y)\right) + \cos\left(\frac{2\pi}{p}(x-y)\right) \right] \right\}. \quad (2)$$

The propagation of light in space can be represented by complex amplitude.

$$A(r) = \sqrt{I(r)} \exp[i(kr - \varphi(r))], \quad (3)$$

where r is the spatial vector, k is wave vector, I is intensity, and φ is phase. Each diffraction order was propagated along the direction of the wave vector. Then, the optical field propagated a distance z along the z -axis. Because of its free space, diffraction in the premise of paraxial propagation is negligible; the light field at z is superimposed at all diffraction orders. The light field intensity is

$$I(r, z) = I_0 \left\{ 1 + \left[\cos \left(\frac{2\pi}{p}x + \frac{\lambda}{p}z \frac{\partial \varphi(r)}{\partial x} \right) + \cos \left(\frac{2\pi}{p}y + \frac{\lambda}{p}z \frac{\partial \varphi(r)}{\partial y} \right) \right] + \frac{1}{2} \left[\cos \left(\frac{2\pi}{p}(x+y) + \frac{\lambda}{p}z \frac{\partial \varphi(r)}{\partial(x+y)} \right) + \cos \left(\frac{2\pi}{p}(x-y) + \frac{\lambda}{p}z \frac{\partial \varphi(r)}{\partial(x-y)} \right) \right] \right\}, \quad (4)$$

where I_0 is the maximum intensity of the interference pattern in case $z = 0$, φ is the phase of the incident light, and λ is the wavelength of the incident light.

III. DEMODULATION ALGORITHM

After obtaining the interferogram, we will be able to demodulate the phase image of the wavefront. We can calculate the offset of each point to fit the wavefront. FFT analysis proposed in 1982 by Takeda [24] can also be used. The Fourier spectrum of Eq. (4) is

$$U(f_x, f_y) = 2\pi I_0 \left\{ \delta(f_x, f_y) + \frac{1}{2} \left[\delta \left(f_x + \frac{1}{p}, f_y \right) \mathcal{F} \left\{ e^{-i \frac{\lambda}{p} z \frac{\partial \varphi(r)}{\partial x}} \right\} - \delta \left(f_x - \frac{1}{p}, f_y \right) \mathcal{F} \left\{ e^{i \frac{\lambda}{p} z \frac{\partial \varphi(r)}{\partial x}} \right\} \right] + \frac{1}{2} \left[\delta \left(f_x, f_y + \frac{1}{p} \right) \mathcal{F} \left\{ e^{-i \frac{\lambda}{p} z \frac{\partial \varphi(r)}{\partial y}} \right\} - \delta \left(f_x, f_y - \frac{1}{p} \right) \mathcal{F} \left\{ e^{i \frac{\lambda}{p} z \frac{\partial \varphi(r)}{\partial y}} \right\} \right] + \frac{1}{4} \left[\delta \left(f_x + \frac{1}{p}, f_y + \frac{1}{p} \right) \mathcal{F} \left\{ e^{-i \frac{\lambda}{p} z \frac{\partial \varphi(r)}{\partial(x+y)}} \right\} - \delta \left(f_x - \frac{1}{p}, f_y - \frac{1}{p} \right) \mathcal{F} \left\{ e^{i \frac{\lambda}{p} z \frac{\partial \varphi(r)}{\partial(x+y)}} \right\} \right] + \frac{1}{4} \left[\delta \left(f_x - \frac{1}{p}, f_y + \frac{1}{p} \right) \mathcal{F} \left\{ e^{-i \frac{\lambda}{p} z \frac{\partial \varphi(r)}{\partial(x-y)}} \right\} - \delta \left(f_x + \frac{1}{p}, f_y - \frac{1}{p} \right) \mathcal{F} \left\{ e^{i \frac{\lambda}{p} z \frac{\partial \varphi(r)}{\partial(x-y)}} \right\} \right] \right\}, \quad (5)$$

where δ is the Dirac function, \mathcal{F} represents the Fourier transform, $i = \sqrt{-1}$.

As shown in Eq. (5), the interferogram spectrum can be divided into nine parts from the difference of the center frequency, corresponding to the nine regions in Fig. 2, which is located in the center of the zero-order spectrum corresponding to the incident light intensity distribution. Ideally, the incident light intensity is constant, which means the spectral width of the zero-order is 0. The remaining eight regions represent first-order spectral information, each center located at $\left(\pm \frac{1}{p}, \pm \frac{1}{p}\right)$, $\left(0, \pm \frac{1}{p}\right)$, and $\left(\pm \frac{1}{p}, 0\right)$. The first-order spectrum of the interferogram corresponds to the modulated information of the interference fringes, including the phase gradient of the incident wavefront. We used a filtering window at frequency domain to extract the first-order spectrum of the interferogram. Then, we moved the center of the first-order spectrum to $(0, 0)$ in the coordinates and took an inverse Fourier transform.

$$A(x, y) = \mathcal{F}^{-1} \left\{ \delta(f_x, f_y) \mathcal{F} \left\{ e^{-i \frac{\lambda}{p} z \frac{\partial \varphi(r)}{\partial x}} \right\} \right\} = e^{-i \frac{\lambda}{p} z \frac{\partial \varphi(r)}{\partial x}}, \quad (6)$$

where \mathcal{F}^{-1} represents the inverse Fourier transform.

$A(x, y)$ in Eq. (6) contains a phase gradient in certain direction. Then we can obtain a phase gradient in the x direction.

$$\begin{aligned} \frac{\partial \varphi(r)}{\partial x} &= -\frac{p}{\lambda z} \text{Angle}[A(x, y)] \\ &= -\frac{p}{\lambda z} \arctan \left\{ \frac{\text{Imag}[A(x, y)]}{\text{Real}[A(x, y)]} \right\}, \end{aligned} \quad (7)$$

where $\text{Angle}[A(x, y)]$ means take the phase angle of complex $A(x, y)$. $\text{Imag}[A(x, y)]$ means obtain the imaginary part of $A(x, y)$, and $\text{Real}[A(x, y)]$ means obtain the real part of $A(x, y)$.

Similarly, we got the phase gradient $\frac{\partial \varphi(r)}{\partial y}$ by extracting the first-order spectrum, of which the center is located at the point $\left(0, \frac{1}{p}\right)$. After we got the phase gradient along both the x axis and the y axis, the phase image of the wavefront can be rebuilt by the Fourier integral method. The reconstruction equation is

$$\varphi(r) = \mathcal{F}^{-1} \left[\frac{\mathcal{F} \left(\frac{\partial \varphi(r)}{\partial x} \right) + i \mathcal{F} \left(\frac{\partial \varphi(r)}{\partial y} \right)}{f_x + i f_y} \right]. \quad (8)$$

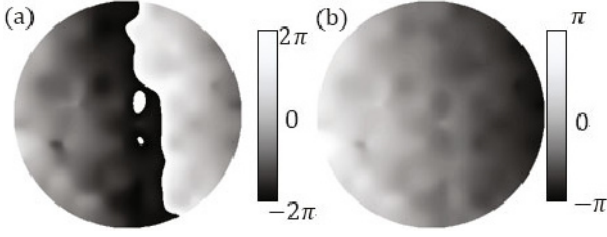


Fig. 3. A wrapped wavefront gradient in case of tile (a) and its proper value (b).

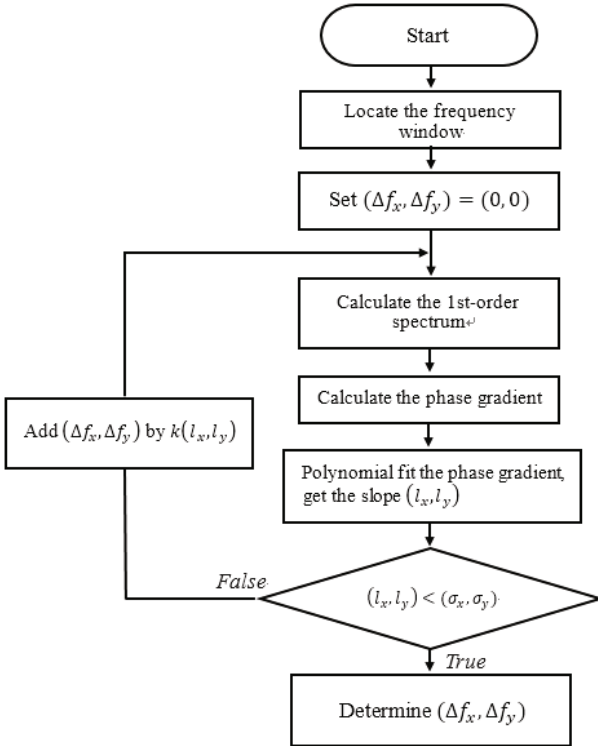


Fig. 4. Flowchart of the iterative calibration algorithm.

IV. PHASE-SHIFTING ITERATION ALGORITHM

In practice, the interferogram and its Fourier transform are all represented as a matrix of discrete numbers. MHM usually has an angle of rotation to CCD. Therefore, the first-order spectrum center tends not to be located at the integer coordinate positions. If we directly select the location of the nearest neighbor of the center to calculate, it will result in some tilt at the phase gradient, even resulting a wrapped phase, as shown in Fig. 3.

Using the numeric operation to unwrap the wavefront gradient will make it difficult to obtain the proper result in case of the noise. Therefore, we developed an iterative phase-shifting algorithm to solve this problem. First, select the nearest neighbor of the spectrum center and take the operation described by Eq. (6). When the center we selected is close enough to the actual center, the phase

gradient we got will not be wrapped but will be inclined. In the next step, we will fit the inclined gradient to provide a slope. Then, we can determine the offset of the center from the slope. After several iterations, the central location will become quite accurate.

According to the Fourier shift theorem, phase shifting of a function in the spatial domain will result in translation in the frequency domain.

$$\mathcal{F}\{g(x, y) \exp[i2\pi(f_a x + f_b y)]\} = G(f_x - f_a, f_y - f_b). \quad (9)$$

According to Eq. (9). We need to multiply an appropriate correction at the inverse Fourier transform of the phase gradient to eliminate the non-integer offset of the spectrum center. Then, the inclination will be eliminated, and we can get the proper wavefront gradient.

Therefore, we must calibrate the interferometer to prevent a wrong result. The center of the first-order spectrum must coincide with the center of the frequency domain window.

Suppose the incident light is an ideal plane wavefront. The frequency spectrum of the wavefront is

$$U(f_x, f_y) = \delta(f_x, f_y). \quad (10)$$

If the center of the selected window does not coincide with the first-order spectrum center. Suppose the offset is $(\Delta f_x, \Delta f_y)$. Then $U'(f_x, f_y) = U(f_x - \Delta f_x, f_y - \Delta f_y)$. There will be

$$\frac{\partial \varphi'(x, y)}{\partial x} = 2\pi(\Delta f_x x + \Delta f_y y). \quad (11)$$

By Eq. (11), the offset between the center of the selected window and the center of the first-order spectrum will cause linear tilt in the obtained phase gradient. Next, a polynomial fitting method will be used to calculate the tilt factor. Then the offset will be estimated between two centers. It should be noted that the arc-tangent function range is $[-\pi, \pi]$. If the phase gradient didn't wrap. There must be

$$|2\pi(\Delta f_x x + \Delta f_y y)| < \pi. \quad (12)$$

The interferogram is represented as a discrete size $M \times N$ matrix. Then, the spectrum of the two-dimensional Discrete Fourier Transform can be expressed as

$$F(u, v) = \sum_{x=0}^{M-1} \sum_{y=0}^{N-1} f(x, y) e^{-j2\pi(\frac{ux}{M} + \frac{vy}{N})}, \quad (13)$$

where $u = 0, 1, \dots, M-1$ and $v = 0, 1, 2, \dots, N-1$.

By Eqs. (12) and (13), there will be

$$\Delta f_x M + \Delta f_y N < \frac{1}{2}. \quad (14)$$

The frequency difference between two adjacent pixels in the spectrum is $(\frac{1}{M}, \frac{1}{N})$. The pixel difference between the selected center and the actual center should be no more than 0.5.

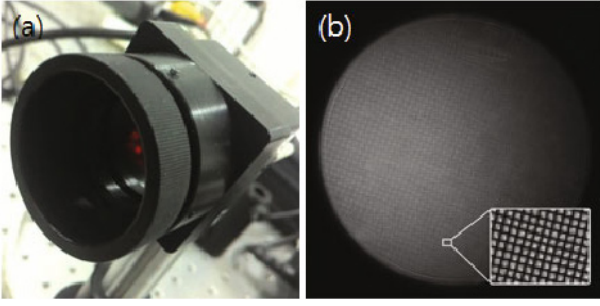


Fig. 5. (Color online) Quadriwave lateral shearing interferometer image (a) and its interferogram (b).

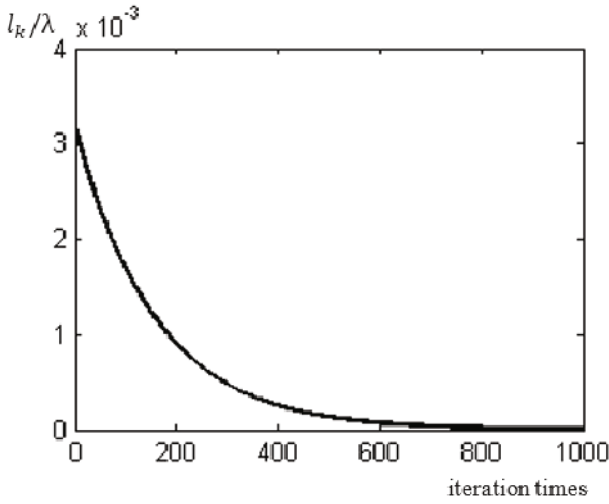


Fig. 6. The relation curve of l_k and iteration number.

We can calculate the tilt of the gradient image by using the polynomial fitting method. Then, the offset value of the spectrum window center can be fixed. Repeat this process several times until the remaining tilt is less than the threshold. The flowchart about the iteration process is shown in Fig. 4.

V. EXPERIMENTAL RESULTS

The quadriwave lateral shearing interferometer is shown as Fig. 5(a). It includes an MHM and a CCD. First, etch the MHM pattern on the photoresist layer using laser direct writing process. Then transfer the pattern of the photoresist layer onto a glass substrate by using the reactive ion beam etching technology. The aperture period of the Hartmann diaphragm p is $11\ \mu\text{m}$, and the CCD pixel size is $5.5\ \mu\text{m}$. The resolution of CCD is 2048×2048 , which means the maximum resolution of phase image is 512×512 . Figure 5(b) is an interferogram obtained by this shearing interferometer.

To verify the calibration algorithm, we use a collimator to generate plane wavefront. Using the calibration process shown in Section 4, we obtained a series of ex-

Table 1. Contrast of the average of wavefront RMS before and after calibration.

Iteration number	RMS before calibration	RMS after calibration
1000	0.005λ	$6.1 \times 10^{-5}\lambda$
1000	0.020λ	$1.1 \times 10^{-4}\lambda$
1000	0.080λ	$1.3 \times 10^{-4}\lambda$
1000	0.200λ	$1.5 \times 10^{-4}\lambda$
1000	0.500λ	$1.4 \times 10^{-4}\lambda$

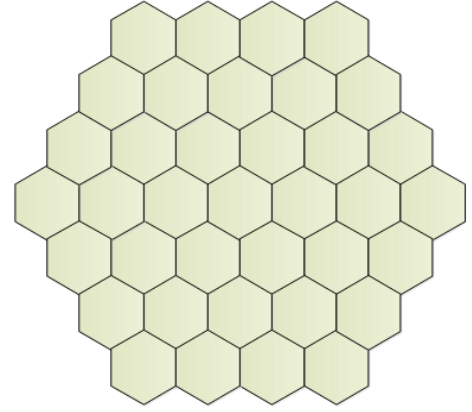


Fig. 7. A type map of PT111-5 segmented MEMS deformable mirror.

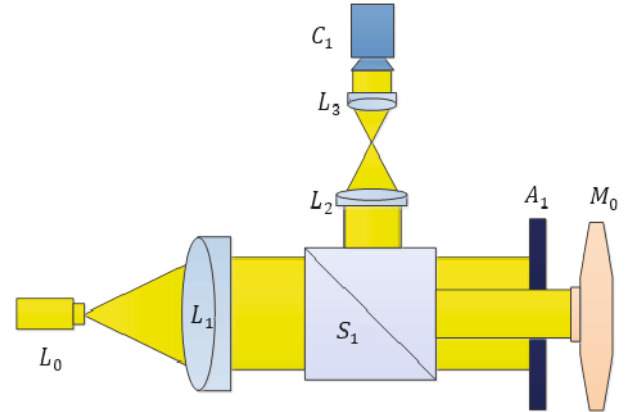


Fig. 8. (Color online) Optical path of quadriwave lateral shearing interferometry experiment.

perimental results. We choose $k = 0.8$ to do a phase-shifting iterative experiment. Then, we obtained the statistics of the residual value $l_k = \sqrt{(l_x^2 + l_y^2)}$. As shown in Fig. 6, when the number of iterations reaches at least 1000, change of l_k has been stabilized.

To ensure the validity of the experimental results, we performed multiple sets of calibration experiments. We use a series of incremental RMS values of the test and acquire the data in the table. As shown in Table 1, the experimental results show that the proposed phase-shifting

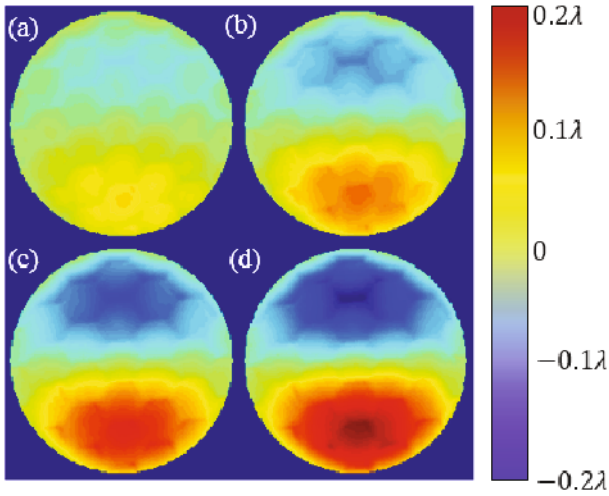


Fig. 9. (Color online) Y axis coma with different RMS obtained by quadriwave lateral shearing interferometer. (a)0.05 λ ; (b)0.10 λ ; (c)0.15 λ ; (d)0.20 λ

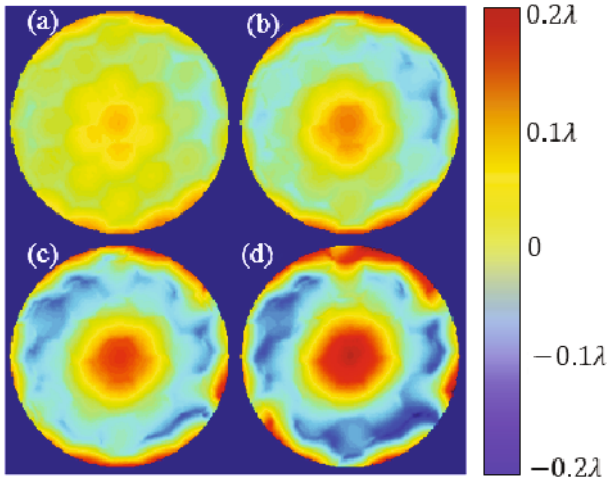


Fig. 10. (Color online) Spherical aberration with different RMS obtained by quadriwave lateral shearing interferometer. (a)0.05 λ ; (b)0.10 λ ; (c)0.15 λ ; (d)0.20 λ

iteration algorithm can reduce the error of the wavefront gradient RMS to $1.5 \times 10^{-4}\lambda$, which meets the requirements of the wavefront detection accuracy.

We use 632.8 nm fiber source with 37 units segmented deformable mirror produced by Iris AO to generate the wavefront. The maximum stroke of the mirror unit is 8 μm , and the maximum frame rate is 6.5 kHz. The type of deformable mirror surface is shown in Fig. 7, wherein each hexagon is a single 4 degrees of freedom mirror unit.

The optical path is shown in Fig. 8.

Each variables in Fig. 8 represents: L_0 : 632.8 nm fiber source, S_1 : 20mm dispersion prism, L_1 : 10mm lens, L_2 : 7mm lens, L_3 : 5mm lens, A_1 : 5mm diameter pupil aperture stop, M_0 : MEMS deformable mirror, C_1 : Contrast wavefront sensor.

Figures 9 and 10 shows the results of the reconstructed

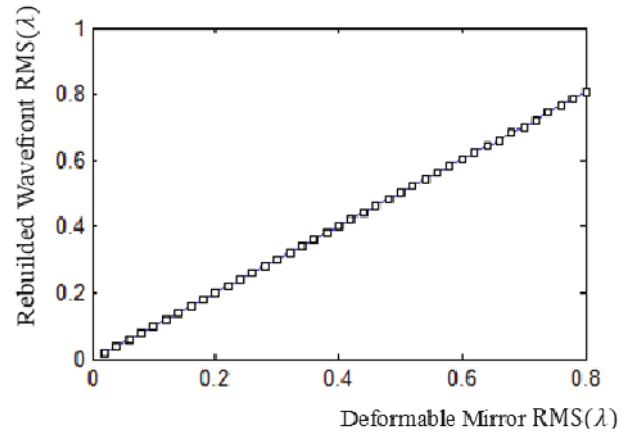


Fig. 11. Contrast of reconstructed wavefront RMS and deformable mirror RMS.

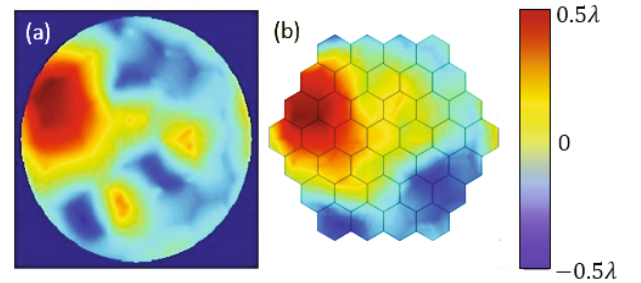


Fig. 12. (Color online) Contrast of reconstructed wavefront (a) and deformable mirror graph (b).

wavefront produced by MEMS.

We use MEMS deformable mirror to produce a relatively RMS from 0.02 - 0.8 range of defocus wavefront. Figure 11 is the contrast between deformable mirror RMS and reconstructed wavefront RMS detected by QWLSI. The linear fitting error is less than 1.5×10^{-2} . Thus, after the iterative algorithm calibration, our QWLSI gets the reliable phase image.

Finally, we use MEMS deformable mirror to produce a random wavefront. Figure 12 shows the contrast between the reconstructed wavefront detected by QWLSI and the wavefront graph of the deformable mirror. The covariance between two wavefronts is 2.63%. This is a quite ideal result considering there're some deviation in the non common optical path.

Experimental results showed that the proposed phase shifting iterative calibration algorithm used by quadriwave lateral shearing interferometry can effectively eliminate the tilt error. This algorithm improved the calculation accuracy and had important significance and application value in wavefront sensing and analysis of interferogram.

VI. CONCLUSION

A phase-shifting iterative algorithm is proposed to calibrate the wavefront phase image demodulated from an interferogram generated using quadriwave lateral shearing interferometry. We take a reverse iteration to pinpoint the location of the first-order spectrum center, reducing the tilt error brought by the special window. From the experimental wavefront detection result, we can summarize that this algorithm improves the accuracy of the phase image. So that the QWLSI can achieve the desired result. The next stage of our research will focus on the reconstruction algorithm for image restoration of the wavefront. And to meet the high-speed, low consumption of resources for the purpose of the high-efficiency precision wave reconstruction algorithm.

REFERENCES

- [1] J. C. Chanteloup, *Appl. Opt.* **44**, 1559 (2005).
- [2] J. Primot and N. Gurineau, *Appl. Opt.* **39**, 5715 (2000).
- [3] J. C. Chanteloup and M. Cohen, *Proc. SPIE* **5252**, 282 (2004).
- [4] S. Velghe *et al.*, *Proc. SPIE* **5965**, 12 (2005).
- [5] J. Rizzi *et al.*, *Opt. Lett.* **36**, 1398 (2011).
- [6] M. Hasegawa *et al.*, *Proc. SPIE* **5533**, 27 (2004).
- [7] S. Kato *et al.*, *Proc. SPIE* **110**, 5751 (2005).
- [8] K. Sugisaki *et al.*, *Proc. SPIE* **1**, 5921 (2005).
- [9] S. Velghe *et al.*, *Proc. SPIE* **7113**, 0X (2008).
- [10] S. Velghe *et al.*, *Proc. SPIE* **7300**, 0T (2009).
- [11] W. Boucher *et al.*, *Proc. SPIE* **9633**, 1T (2015).
- [12] S. Mousset *et al.*, *Opt. Lett.* **31**, 2634 (2006).
- [13] C. Bellanger *et al.*, *Opt. Lett.* **23**, 3931 (2011).
- [14] P. Bon *et al.*, *Opt. Express* **17**, 13080 (2009).
- [15] G. Baffou *et al.*, *ACS Nano* **3**, 2452 (2012).
- [16] S. Aknoun *et al.*, *Opt. Express* **12**, 16383 (2015).
- [17] Y. Xiumei *et al.*, *Chin. J. Lasers* **10**, 1008006 (2015).
- [18] T. Ling *et al.*, *Sci. Rep.* **1**, 9 (2017).
- [19] K. Hibino *et al.*, *J. Opt. Soc. Am. A* **4**, 761 (1995).
- [20] P. S. Huang *et al.*, *Appl. Opt.* **22**, 4503 (2002).
- [21] P. Bing *et al.*, *Opt. Lett.* **4**, 416 (2009).
- [22] S. Zwick *et al.*, *Proc. SPIE* **8169**, 241 (2011).
- [23] S. Zwick *et al.*, *Appl. Opt.* **14**, 3134 (2013).
- [24] M. Takeda *et al.*, *J. Opt. Soc. Am.* **72**, 156 (1982).